Advancing interpretation of incoherent scattering in ice penetrating radar data used for ice core site selection

Ellen Mutter[1] and Nicholas Holschuh[2]

[1]Department of Earth and Atmospheric Sciences, Cornell University, Ithaca, NY, 14853, USA
[2]Department of Geology, Amherst College, Amherst, MA 01002, USA

Correspondence to: Nicholas Holschuh (nholschuh@amherst.edu)

Abstract. Below the coherent layering in ice penetrating radar data collected in Antarctica and Greenland, incoherent scattering is common. This scattering is signal, not noise, and has the potential to inform our understanding of the structure and dynamics of the bottom 20% of glaciers and ice sheets. Here, we present a comparison between radar imagery and ice core properties for seventeen ice core sites across Antarctica and Greenland, to identify possible sources for incoherent scattering and evaluate its use in ice core site selection. We find that incoherent scattering is commonly coincident with either gradual changes in crystal orientation fabric or rapidly fluctuating fabrics in deep ice, where strain is localized by strength differences associated with ice grain size. Macro-scale deformation and layer folding at scales below the range-resolution of radar does not seem to result in incoherent scattering or induce an echo free zone, as has been previously hypothesized. Where incoherent scattering is laterally homogeneous in intensity, layering is typically undisturbed in nearby ice cores. But where incoherent scattering is laterally heterogeneous in intensity and the pattern does not appear conformal with subglacial topography, we find multi-meter-scale folding and associated discontinuities in nearby ice core records. Future higher-resolution sampling of fabric in ice cores would allow for more quantitative interpretation of incoherent scattering and its amplitude, but we show that the qualitative nature of incoherent scattering has the potential to inform us about the continuity of climate records at prospective ice core sites and should be considered when evaluating the nature and quality of basal ice.

1. Introduction

Existing ice cores provide our best record of past atmospheric chemistry. These cores capture global climate changes over the Holocene and Late Pleistocene (Wolff et al., 2010). Future ice coring initiatives hope to build on that record, both extending it further back in time (Jouzel and Masson-Delmotte, 2010) and measuring regional climate change (Mulvaney et al., 2021) during specific climate periods (Fudge et al., 2023). These future projects focus on the identification and collection of very specific ice, and so they typically start with extensive geophysical surveying for "site selection" preceding drilling. Ice penetrating radar data have served as the primary tool for this work, which uses layering in radar imagery to infer spatially variable accumulation, basal melting, and ice flow, and through that, identifying ideal ice core sites (Bingham et al., 2024; Chung et al., 2023, Karlsson et al., 2018; Schroeder et al., 2020). But site selection has relied primarily on the strong, coherent signal that spans the upper three-quarters of the ice column in most radar imagery. Here we focus on improving interpretation

32 of other signals in radar data, with a particular focus on what deep incoherent scattering (described in section 2) can tell us
33 about ice near the ice sheet base.

34 All radio-wave scattering in ice originates from dielectric contrasts. To better understand the nature and sources of scattering
35 in existing ice penetrating radar data, several previous studies have compared radar imagery to observations of ice chemistry
36 and physical properties measured in ice cores (e.g., Eisen et al., 2003, 2007; Hammer, 1980; Harrison, 1973; Millar, 1982;
37 Mojtabavi et al., 2022). But that work has focused on the coherent, isochronal layering, and comparatively little has been done
38 to understand the deeper signals, which are becoming better sampled with modern, high power / low noise systems. This deep
39 ice has also become increasingly scientifically important, as it is at the center of the search for an ice core record that spans
40 the Mid-Pleistocene transition (Chung et al., 2023; Lilien et al., 2021). Using data from 17 ice cores across Antarctica and
41 Greenland (Fig. 1), we work to better understand the physical properties that produce deep, incoherent scattering, and evaluate
42 the extent to which it may be diagnostic of layer disturbances or other disqualifying characteristics when pursuing future ice
43 cores.
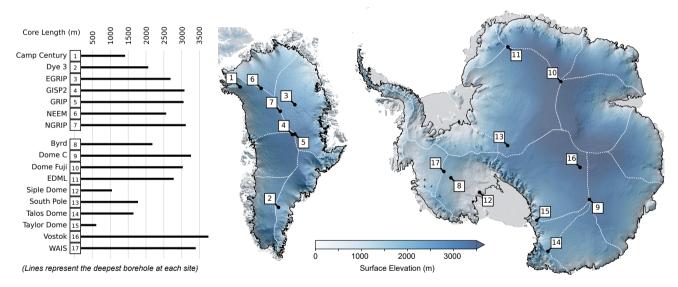
44
45 **Figure 1: Locations of major ice coring initiatives in Greenland and Antarctica used in this study and the lengths of the associated**
46 **cores. Surface elevation maps of Antarctica** (Howat et al., 2019) **and Greenland** (Porter et al., 2018) **with catchment boundaries**
47 (Mouginot and Rignot, 2019; Rignot et al., 2013) **showing ice divides in white.**

2. Background: Scattering and the Radar Imaging Problem

49 Radar systems actively transmit energy into the subsurface. Time-of-flight measurements for back-scattered energy (together
50 with a known speed of light in ice) can be used to infer the position of subsurface scatterers and reconstruct the geometry of
51 glacier systems (Bingham et al., 2024; Dowdeswell and Evans, 2004). In the near sub-surface, contrasts in the dielectric

permittivity that scatter energy are controlled primarily by variations in density, while most deeper englacial reflectors arise from either conductivity contrasts, due to variations in the concentration of free ions deposited with the snow at the surface (Stillman et al., 2013), or transitions in the ice crystal fabric, typically localized by changes in grain size also arising from impurity deposition (Fujita et al., 1999). Fabric induced scattering is a product of the dielectric anisotropy of individual ice crystals, with transitions in c-axis fabric capable of producing an (up to) ~1.3% contrast in the polarization-dependent bulk permittivity (Matsuoka et al., 1997). Incoherent scattering may come from both chemical and physical sources; we work to provide some of the first constraints on its origins here.

Glaciologists primarily use radar data for ice core site selection in two ways. The first approach is focused on the geometry of coherent, isochronous layering within the ice sheet (an example of which can be seen in the upper portions of Fig 2.a). These layers originate as flat-lying layers of snow at the ice sheet surface and are transformed by flow during burial; thus, their geometry can be used to diagnose spatial variations in accumulation (e.g., Karlsson et al., 2020), glacier sliding (e.g., Leysinger Vieli et al., 2007), and basal melt (e.g., Bingham et al., 2024; Fahnestock et al., 2001). The second approach is focused on the nature of subsurface scattering, both its coherence (e.g., Lindzey et al., 2020; Oswald et al., 2018; Schroeder et al., 2015) and amplitude (e.g., Catania et al., 2003; Christianson et al., 2016; Chu et al., 2018), which together can be used to infer the modern electrical (and, more generally, material) characteristics of the ice sheet and its substrate.

Subsurface targets can be divided into two main categories: specular interfaces and rough (or diffuse) scatterers (Schroeder et al., 2015). Specular interfaces, like mirrors, scatter energy in one dominant direction, a function of the direction-of-arrival for the incoming radio wave and the orientation of the interface. Diffuse scatterers redistribute incident energy at a variety of angles. This leads to significant differences in the coherence of the scattering between specular and diffuse targets (defined here as the consistency in phase and amplitude of the backscattered energy with slight changes in the position of the radar system). Incoherent scattering typically occurs at rough interfaces or when there are multiple diffuse scattering targets at a similar range from the instrument. It has been observed as a product of rare glacier conditions, for example, where there is significant temperate ice and associated englacial water (Hamran et al., 1996) or where debris has been entrained near the base of glaciers (Winter et al., 2019). But it must also be generated by more common glaciological phenomena, as it is present within several hundred meters of the ice sheet base across large parts of Antarctica and Greenland.

Consider the example radar image in Fig. 2.a. Each pixel represents either backscattered energy or electrical or thermal noise in the radar electronics. The position of the radar system varies across the columns in the image, and the delay-time following the transmitted pulse (associated with the range to possible targets) varies across the rows in the image. In regions dominated by planar, specular interfaces (as in the upper half of Fig. 2.a), each pixel typically represents backscattered energy from only a single direction of arrival. This is because, even though there are many scattering targets at the range associated with that pixel (as shown in Fig. 2.b), only that interface tangential to the range shell (such that the interface is normal to the propagating

wave) returns energy to the system. But in regions where there are diffuse scatterers, each pixel in a radar image represents the interference of scattering from multiple targets, with backscattering arriving from multiple angles (Fig. 2.b.ii/iii). With slight changes in the position of the system, the dominant source of scattering at a given range can change, resulting in little consistency in phase or amplitude from pixel to pixel. This is extremely common for energy arriving below the ice bottom reflector, with a long tail of incoherent scattering appearing at greater range (Fig. 2.a.iii). Less well described is incoherent scattering from within the ice column (Fig. 2.a.ii) which is the focus of our research here.

When considering the nature of scattering in radar imagery, it is important to remember that the images themselves are ultimately a product of three things:

1. The geometry and physical / electrical characteristics of the glacier subsurface.
2. The system used to collect the data (including the characteristics of the transmitted wave, antennas, and transmit / receive electronics).
3. The filtering, focusing, and additional image processing algorithms applied after collection.

The nature of radar targets depends on both the scale of electromagnetic heterogeneity in the medium and the frequency content of the transmit pulse (with higher frequencies / bandwidths associated with finer range resolution). This is because the specularity of a target is ultimately dictated by the Rayleigh roughness criterion for an interface, with specular scattering occurring when roughness elements are less than $1/8^{th}$ the scale of the dominant radar wavelength (Peters et al., 2005). Figure 2.c demonstrates how the same targets manifest differently across different radar systems; with lower resolution systems, scattering appears more structured, like the specular and coherent layering in the shallow ice.
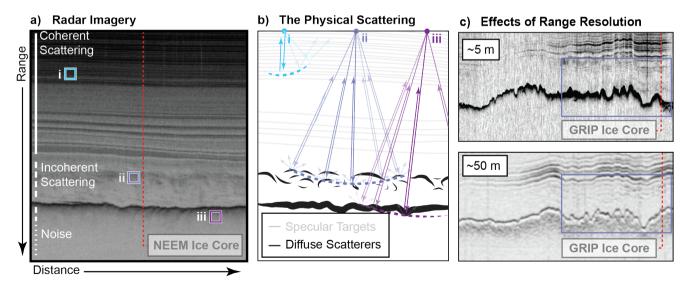
Figure 2: (a) Example radar image, (b) the ray-paths associated with scattering targets that contribute to individual pixels in the radar imagery, and (c) a pair of images highlighting the effect of system characteristics on the nature of deep scattering. Profiles presented in panel (c) were collected along sub-parallel tracks adjacent to the GRIP Ice Core site. Radar system characteristics for radargrams in (a) and (c) can be found in Supplementary Table 1.

To generate incoherent scattering, deep ice must differ from the planar, layered structure of the shallow ice column in some way. It may be that incoherent scattering occurs because chemical layering is mechanically disturbed in the deep ice and is no longer planar. Or, it may be that other processes (like dynamic recrystallization or grain rotation) acting locally (due to enhanced stress near obstacles to flow, transitions in the basal thermal state, or fluidity contrasts in the ice) introduce lateral heterogeneity in physical properties that produce incoherent scattering (Gerber et al., 2024). Here, we compile radar data from a variety of geophysical campaigns, including ground-based and airborne surveys conducted by the Center for Remote Sensing and Integrated Systems (CReSIS), the British Antarctic Survey (BAS), the University of Texas (UT), the University of Washington (UW), and the Alfred Wegener Institute (AWI) – (see Supplementary Table 1 for full system characteristics). From those data, we analyze representative, ice core adjacent radar images, and compare them to measurements of crystal orientation fabric and micro- and macro-scale structures, to test two hypotheses:

1. That transitions in ice COF are collocated with (and likely induce) incoherent scattering.
2. That small scale deformation of chemically distinct layering can induce incoherent scattering.

We are drawing from heterogeneous, historical data, which can make imagery intercomparison difficult. Because some systems used for site selection do not preserve phase information, we focus primarily on the amplitude and character of scattering, controlling for differences in system characteristics. Differences in image processing also have the potential to modify the expression and amplitude of incoherent scattering. Therefore, an important caveat of this work is that our interpretation of incoherent scattering only holds for imagery collected with radar hardware typical of the earth 2000's (with center frequences in the 100s of MHz) and the most common image post-processing (SAR focusing and along-track multilooking).

3. Data and Methods: Measurements Capturing the Fine- and Large-Scale Electrical Structure of Ice Cores

Folds and layer disturbances at all scales have been observed or inferred from ice core records in both Antarctica and Greenland. Some scales of folding are more easily detected – millimeter and centimeter scale folds can be measured directly within the 8-13 cm diameter ice cores. Folding at the 100s of meters scale is resolvable by radar. But all scales in between must be inferred using anomalous patterns of electrical conductivity, stable isotope or impurity concentrations, or physical and optical properties. We summarize the measurements that we use to identify deformation in deep ice below, and aim to relate radio-wave scattering phenomena to these observations.

Physical analysis of ice cores, including macro-scale visual observations and optical imaging (i.e. linescanners) (Faria et al., 2018; Jansen et al., 2015; Svensson, 2005), and alternating current and direct current electrical conductivity measurements (ECM) (Fudge et al., 2016; Wolff, 2000) provide the best direct measurement of small-scale features deep in the ice column. The resolution of typical linescan images is around 0.1 mm/pixel, allowing for observations of layers and their structure ranging from millimeter-scale undulations up to folds at the scale of the typical diameter of deep ice cores (Fig. 3). Data from ice core linescanning have shown wavy strata (e.g. WAIS -- West Antarctic Ice Sheet Divide (Fitzpatrick et al., 2014)), highly inclined

strata (e.g. EDML -- EPICA Dronning Maud Land (Faria et al., 2018)), duplex and boudin-like structures (e.g. EastGRIP (Westhoff, 2021)), 10 cm-scale z-folds (e.g. NEEM -- North Greenland Eemian Ice Drilling (Jansen et al., 2015)), diffuse layering (e.g. NorthGRIP (Svensson et al., 2005)), and extreme growth of individual ice grains reaching diameters of up to 50 cm (e.g. EDML (Faria et al., 2018)), capturing unique forms of stratigraphic disturbance and in some cases, informing the depth associated with discontinuities in the climate record (Fig. 4).

To supplement imaging methods that capture small scale deformation, a range of chemical methods have been employed across deep ice core sites to identify major breaks in stratigraphic continuity and large-scale folding. Some breaks in continuity have been identified using chemical disagreement between ice cores. For cores in the same geographic region (e.g. GISP2 -- Greenland Ice Sheet Project Two, GRIP -- Greenland Ice Core Project, and NorthGRIP -- North Greenland Ice Core Project), divergence in electrical conductivity, $\delta^{18}O$ of ice ($\delta^{18}O_{ice}$), and impurity concentrations can be used to identify the onset of a discontinuous record (Johnsen et al., 2001). When looking across hemispheres, divergence in the profiles of globally well-mixed $\delta^{18}O$ of atmospheric O_2 ($\delta^{18}O_{atm}$) and CH_4 have been used to identify climate record discontinuity (Chappellaz et al., 1997; Landais et al., 2003). In cases where there are no cores that provide high resolution comparison, sudden shifts in the nature of the chemical signal (e.g. changes in
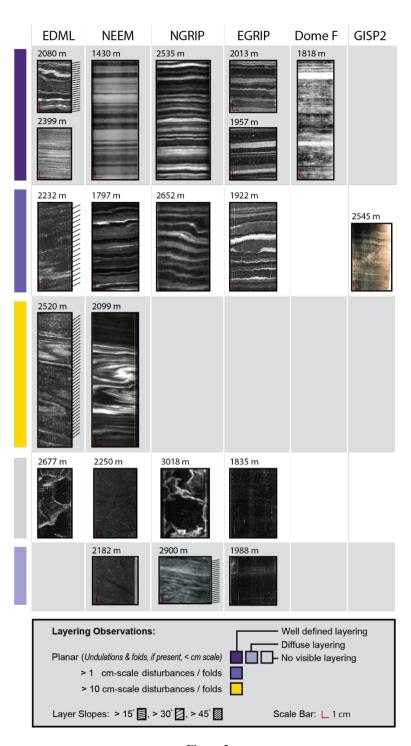
Figure 3

Figure 3: Examples of linescan images capturing mm to >10-cm scale deformational structures. Microinclusion-rich ice strata scatter light creating bright horizons, or cloudy bands, revealing stratigraphic structure. Well-defined planar layering with mm-scale undulations is observed in all cores with available linescan images. Cm-scale deformational structures include z-folds (EDML and GISP2), cm-scale undulations (NEEM and NorthGRIP), and boudin-like structures (EastGRIP). Overturning folds that span over 10 cm of the ice column are observed at EDML and NEEM. Ice without layer structure can be due clear ice that lacks sufficient microinclusions for scattering (NEEM and EastGRIP) as well as ice with large individual crystal grains (EDML and NorthGRIP). Diffuse or weak layering is observed when microinclusions are minimal (NEEM and EastGRIP) or lacking clear layer structure (NorthGRIP). Linescan data is sourced from Faria et al., 2018 (EDML), Takata et al., 2004 (Dome Fuji), Kipfstuhl, 2009 (NEEM), Svensson, 2005 (NorthGRIP), Alley et al., 1997 (GISP2), Weikusat et al., 2020 (EastGRIP).

chemical variability or abrupt changes in the gas-age ice-age difference, described as either the Δage between the ice and gas or the depth-shift separating gas and ice of a constant age) have been used to infer climate record discontinuities (Crotti et al., 2021; Dansgaard, 1982; Jouzel et al., 2007; Petit et al., 1999; Ruth et al., 2007). Chemical methods have also been used to reconstruct chronologies in heavily disturbed stratigraphy (Landais et al., 2003; NEEM Community Members, 2013; Raynaud et al., 2005; Souchez et al., 2002; Verbeke et al., 2002), and from those chronologies, identify overturned folding. These methods have in some places tentatively inferred (e.g., at Vostok and GRIP) and in other places clearly identified (at NEEM) folding on scales of 10-100 m.

In our analysis, we synthesize the literature on macro-scale stratigraphic disturbances, grouping and analyzing the effect of deformational structures on radar scattering based on reported fold size, slope inclination, and layer visibility. To do this, we identify the depth at which these features are observed (presented in Fig. 4) and compare the observed deformation patterns with collocated radar imagery. Most studies present examples of deformational feature types followed by qualitative descriptions of their frequency throughout the ice column; therefore, the reported ranges should be treated as zones of deformational structures with intermittent occurrence, rather than a continuous span of small-scale deformation.

In addition to measurements capturing the macro-scale, we present crystallographic analysis of glacial ice, typically performed using vertical and / or horizontal thin sections of ice cores. C-axis orientation can be measured with a range of techniques, including polarized light microscopy (Azuma et al., 1999; Weikusat et al., 2017; Wilson et al., 2003), x-ray diffraction and tomography (Miyamoto et al., 2011), sonic wave methods (Kluskiewicz et al., 2017), electron backscatter diffraction microscopy (Obbard and Baker, 2007), and open resonator methods (Saruya et al., 2024). Measurements of the bulk c-axis orientation of glacial ice gives us a direct constraint on how the polarization-dependent permittivity of ice might vary with depth, and therefore how variations in crystal orientation itself may be a source of scattering. C-axis measurements also provide information about the strain history of ice, with implications for larger-scale deformation in the ice column.

Historically, data from thin sections have provided the most robust evidence of differential strain at small scales, capturing fabric changes within a single 10 cm vertical thin section (e.g. NEEM (Montagnat et al., 2014)). But the logistics of thin section sampling limits their ability to capture some scales of vertical and horizontal variability in fabric. The distance between

214 adjacent, discrete thin-section samples can be anywhere from 20 to 100+ m (e.g. EDML (Weikusat et al., 2013), Siple Dome
215 (Gow and Meese, 2007), NorthGRIP (Wang et al., 2002), GRIP (Thorsteinsson et al., 1997)). New approaches to c-axis
216 characterization may change what is possible in future studies of fabric derived scattering, as thick-section open resonator
217 methods have been used to measure the clustering of crystal c-axes every 20 mm along the Dome Fuji core (Saruya et al.,
218 2022, 2024). But for most available data, we are limited in our ability to quantitatively predict scattering from existing fabric
219 measurements, as the magnitude of backscatter depends on the depth-rate-of-change of fabric. Instead, we focus primarily on
220 qualitative comparison of fabric changes with radar images.

221 3. Results: Investigating the Sources of Incoherent Scattering

222 We present measured fabric and structural data together with radar imagery across 10 well sampled cores in Figure 4, and we
223 encourage readers of to refer to Figure 4 often as we describe the relationships between structural data and the radiostratigraphy
224 throughout section 3. In section 3.1, we evaluate the depth-agreement of scattering and known fabric transitions. In section
225 3.2, we evaluate the effect of small- and large-scale deformational structures on radar scattering. A full description of the ice
226 core data used to generate Figure 4 can be found in Supplementary Table 2.

227 3.1 Crystal fabric transitions as a source of incoherent scattering

228 Given the enhanced stresses and therefore higher strain-rates near the base of ice sheets, one might expect monotonic but
229 intensifying fabric development with depth. And at the majority of ice core drill sites, c-axis fabrics transition from a quasi-
230 isotropic c-axis distribution at the top of the ice column to a strong single maximum lower in the column (e.g. Camp Century,
231 Dye-3, GISP2, NEEM, EPICA Dome C (EDC), Talos Dome, GRIP), a product of the typical simple shear near the base of a
232 glacier. Ice cores drilled at flank sites or otherwise away from ice divides often exhibit signs of uniaxial horizontal extension,
233 and thus c-axis fabrics transition from quasi-isotropic to girdle-type fabric and then to a single maximum (e.g. NorthGRIP,
234 Vostok, EDML). But variability in the impurity content (which changes with climate) can intensify fabric development and
235 localize fabric transitions, with fabric strengthening typically coincident with higher impurity content (seen at Byrd (Faria et
236 al., 2014), Camp Century (Faria et al., 2014), Talos Dome (Montagnat et al., 2012), EDC (Durand et al., 2009), NEEM
237 (Montagnat et al., 2014), GISP2 (Gow et al., 1997), and Dye-3 (Langway et al., 1988)).
238
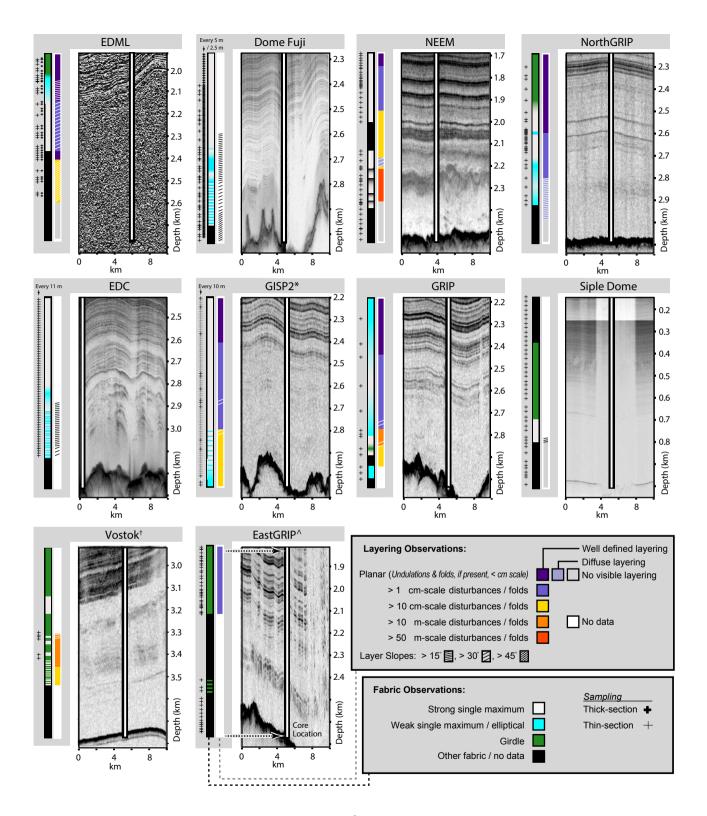
Figure 4: Radargrams capturing deep ice at ice core drill sites with comprehensive fabric and stratigraphic deformation data. From left to right, each ice core panel presents a scatter plot marking sample depths where thin sections, and thick sections where applicable, were collected for crystal orientation fabric analysis, a colormap visualizing of fabric evolution with depth, a colormap visualizing layering evolution and layer slope observations with depth, and a 10 km length radar transect proximal to the ice core drill site. Fabric observations categorized as "other fabric" include multimaxima fabrics (e.g. at EastGRIP and NEEM). Radargrams span the bottom 850 m of each core and 50 m of bedrock. Backscatter power color scales are standardized to span 0.5% to 99% of the return power amplitude recorded in the presented depth range. Radar system characteristics can be found in Supplementary Table 1. The synthesized ice core data includes fabric observations: EDML (Eisen et al., 2007; Faria et al., 2018; Weikusat et al., 2013), Dome Fuji (Saruya et al., 2022, 2024), NEEM (Eichler, 2013; Montagnat et al., 2014), NorthGRIP (Wang et al., 2002), EDC (Durand et al., 2009), GISP2 (Gow et al., 1997), GRIP (Thorsteinsson et al., 1997), Siple Dome (Gow and Meese, 2007), Vostok (Obbard and Baker, 2007), EastGRIP (Stoll et al., 2024); and layering observations: EDML (Faria et al., 2010, 2018), Dome Fuji (Dome Fuji Ice Core Project Members, 2017), NEEM (Jansen et al., 2015), NorthGRIP (Svensson, 2005), EDC (Durand et al., 2009), GISP2 (Alley et al., 1995, 1997; Faria et al., 2014; Gow et al., 1997), GRIP (Alley et al., 1995; Dahl-Jensen et al., 1997; Johnsen et al., 1995; Landais et al., 2003), Siple Dome (Gow and Meese, 2007), Vostok (Lipenkov and Raynaud, 2015; Raynaud et al., 2005; Souchez et al., 2002), EastGRIP (Westhoff, 2021; Stoll et al., 2023). *At GISP2, only some of the sampled thin sections have published data (indicated by the black + symbols), and †at Vostok, the original sampling rate is unpublished, with only a few thin sections and general observations available in the literature. ^At EastGRIP, visual characterization of cloudy bands combines folded features and weak layering into a single group (Stoll et al., 2023). We review the published linescan images at EastGRIP and present approximate depths of these two types of layering in Fig. S4.

Abrupt fabric transitions occur within most ice cores in Greenland (e.g. Camp Century, Dye-3, GISP2, and NEEM), where a significant change in impurity deposition at the Holocene-Wisconsin climate transition drives an abrupt strengthening or transition to a vertical-maximum fabric (Faria et al., 2014). In some places, we see a co-located scattering horizon associated with these abrupt transitions in fabric. At NEEM, a transition from a weak vertical girdle to strong single maximum fabric occurs at 1419 m and is coincident with a diffuse reflector in the radargram (Fig. S1). Similar reflectors appear at isolated fabric transitions in Antarctica as well. At Siple Dome, the c-axis fabric transitions from a vertical girdle to a single maximum at 700 m, with a corresponding diffuse reflector in the radar data. At EDML, the c-axis fabric transition from a vertical girdle to a strong single maximum between 2025 m and 2045 m has been identified as the origin of the reflector at 2035 m (Eisen et al., 2007). These reflectors appear less specular (with trailing energy after the initial arrival) than other isochronous layering within radar imagery.

Where we see well sampled gradual transitions in fabric (spanning 50-100 m of the ice column) we observe both diffuse bands of incoherent scattering as well as laterally heterogeneous incoherent scattering. At EDC, the strong single maximum fabric at 2800 m gradually transitions to a broad single maximum fabric at 2857 m and returns to a strong single maximum fabric at 2900 m (Durand et al., 2009). This fabric transition is roughly coincident with the transition from coherent isochronal strata to a single diffuse incoherent scattering layer observed around 2825 m. At Dome Fuji, the strong single maximum fabric at 2660 m gradually weakens before returning to a strong single maximum fabric again at 2760 m (Saruya et al., 2024). This fabric transition appears roughly coincident with a weak diffuse incoherent scattering layer observed at ~2700 m in the radargram (Fig. S2.a).

In many places, especially where annual layer thickness is compressed significantly at the base of the ice column, alternating fabrics have been observed. At Vostok, from 2700 to 3315 m depth, the core alternates between coarse-grained ice with girdle-type fabric and fine-grained ice with single-maximum fabric every ~100 m (Obbard and Baker, 2007). Within the girdle-type fabric zone between ~3220 and 3315 m, we see weakly banded incoherent scattering (3220 – 3290 m). Between ~3315 and 3450 m, alternations between girdle-type and single-maximum fabric occur approximately every ~20 m (Lipenkov and Raynaud, 2015). This zone of increased fabric alternation overlaps with both the no echo zone between ~ 3290 and 3360 m and the upper depths of a weakly banded incoherent scattering unit (~3360 – 3490 m) in the radargram. At GRIP, each of the five thin sections sampled between 2800 and 2950 m depth show alternating fabrics. At GISP2, coarse-grained layers with fabrics that deviate from the strong single maximum are observed at increasing frequencies below 2800 m (Gow et al., 1997). While interpretation of the GISP2 and GRIP radargrams is challenging below 2800 m, 35 km length radar transects show laterally heterogeneous incoherent scattering in that depth range (Fig. S3).

While it is challenging to describe fabric variability at all scales from thin-sections due to their irregular sampling frequency, the smallest scale of fabric variability has been observed or inferred at centimeter-scales, including at Vostok, EDC, Dome Fuji, and EastGRIP.

- At Vostok, fabric alternations occur at cm-scale wavelengths from 3450 m until the transition from meteoric to accreted ice at 3538 m (Lipenkov and Raynaud, 2015). This overlaps with an echo-free zone in the radargram.
- At EDC, ice below 2800 m consists of alternating layers with high impurity content (consistently presenting strong single maximum fabric) and layers with low impurity content (with an associated broad single maximum fabric). After the gradual transition into and out of a broad single maximum fabric at 2850 m, fabric transitions below 2920 m become more local. High spatial sampling (every 0.5 m) between 2933 and 2955 m revealed fabric alternations between each sample (Durand et al., 2009). Unlike at Vostok where the onset of rapid fabric transitions coincides with the start of the echo free zone, the onset of rapid fabric transitions at EDC is associated with thick and sometimes discontinuous bands of incoherent scattering (2900 – 3050 m) in the radargram.
- At Dome Fuji, cm-scale fluctuations from the single maximum fabric, observed by increases in the standard deviation of $\Delta\varepsilon$ (the difference in the relative permittivity, ε, between vertical and horizontal planes), begin around 2400 m and intensify through the base of the ice column (Saruya et al., 2024). The increase in fabric fluctuations between 2400 and 2650 m has no obvious effect on the coherent continuous layering observed in the radargram. However, the Dome Fuji radargram transitions to a zone of laterally homogenous incoherent scattering at 2900 m. Notably, the precise depth of that transition is difficult to constrain in the radar image, due to the combination of increasing layer inclinations (Dome Fuji Ice Core Project Members, 2017) and strong scattering from borehole fluid in the ice core cavity (Fig. S2).
- At EastGRIP, rapid transitions between vertical girdle and multi-maximum fabrics are observed between 2417 and 2484 m, with a strong multi-maximum fabric established below 2500 m (Stoll et al., 2024). The depth range of the

rapid fabric transitions coincides with a layer-conformal package of incoherent scattering. Banding within the package of incoherent scattering is not layer-conformal, and the bands are defined by laterally traceable, abrupt drops in power with depth (rather than laterally traceable, abrupt increases in returned power as we see in the coherent layering above). We describe these traceable lows in power as "nulls", likely the product of destructive interference in scattered energy returning to the radar from multiple directions. The expression of the nulls in the imagery is polarization dependent (Fig. S4; Nymand, 2024 Fig. 3.5) suggesting that this entire scattering package is a result of the fabric.

At NEEM, four sequences of abrupt and then gradual fabric transitions are linked to large-scale deformation starting at ~2200 m. In this section of the ice core, the same oxygen isotope sequence (and its associated fabric gradient, from multi-maxima fabric to single maximum fabric) is repeated, with abrupt fabric transitions at the boundaries between sequences. This is attributed to overturned folds at the base of the ice column, in part, facilitated by rheologic differences in the ice that also produce the abrupt fabric transitions. At these depths we see strong incoherent scattering that is highly laterally variable. Here, both fabric and larger-scale deformation likely play a significant role in the nature of the scattering, with folding introducing lateral heterogeneity in material properties that has not been identified at other ice core sites.

3.2 Folding as a source of incoherent scattering

Millimeter-scale disturbances are likely present in most deep glacial ice, given their ubiquity in ice cores. But we find little evidence that deformation at that scale impacts the radiostratigraphy directly. In the South Pole Ice Core (SPICEcore), inclined and pinched cloudy bands are observed starting at 1000 m and continue intermittently through the end of the core (Fegyveresi and Alley, 2018) without any noticeable impact on radar scattering. Crystal striping at GISP2 is observed starting at 2200 m, coincident with the onset of small-scale undulations in linescan images (Alley et al., 1997). But similar to SPICEcore, there is no associated change in the nature of radar layering. Millimeter-scale z-folds at GRIP first appear at 2438 m and at 2437 m at GISP2 (Alley et al., 1997), which does coincide with a drop in power of coherent scattering layers. But there is a commensurate drop in the ice conductivity variability associated with changes in dust deposition, which better explains that change. Thus, we rule out millimeter-scale folding as a significant contributor to the radar signal observed at these locations.

Stratigraphic disturbances at the centimeter-scale are apparent in all cores with available data. In previous work, this scale of deformation has been invoked as a mechanism for the "echo free zone", with the idea that folding effectively homogenizes dielectric contrasts at the scale of the resolution of the radar (Winter et al., 2017). At EDML and WAIS Divide, the onset of cm-scale disturbance does appear to be collocated with the apparent echo free zone. In both radar images, however, there is a gradual diminution of returned power with depth. It is possible that measured disturbances do reduce the intensity of back-scatter without eliminating it entirely. But there is laterally-continuous layering (with strong back-scatter intensities) in regions of cm-scale disturbances at NorthGRIP, NEEM, EastGRIP, and GRIP, and in regions with disturbances at the scale of 10 cm

346 at NEEM. Radar data at NEEM show no change in scattering behavior associated with deformation at this scale. This seems

347 to imply that these radar systems (with range-resolutions of 2.8 m to 5 m (Supplementary Table S1)) are insensitive to

348 deformation at this scale.

349

350 Larger scale folding does seem to have an effect on the radiostratigraphy. Deeper in the NEEM core, where chemical analyses

351 reveal six zones of disturbed ice, including two large 50 and 100 m thick folded layers of inverted early glacial ice (NEEM

352 Community Members, 2013), high amplitude but laterally variable incoherent scattering can be seen in the radar imagery.

353 Deformation at this scale, thought to be in part due to rheological differences between the glacial and interglacial ice (NEEM

354 Community Members, 2013), is coincident with a loss of coherent banding in the linescan imagery and an increase in the

355 lateral heterogeneity of intensity in incoherent backscatter. Above 3460 m depth at Vostok, folding is also inferred at the meter

356 scale and larger (Lipenkov and Raynaud, 2015). Similarly, there is incoherent scattering in the image at these depths, although

357 the amplitude of the backscatter is weaker, and lateral heterogeneity less pronounced. Finally, at GRIP, tentative chronological

358 reconstructions of disturbed ice below 2750 m show significant disruption and folding on the scale of 10s of meters between

359 2780 to 2850 m. And while near the ice core, this depth-range corresponds with a unit of weak incoherent scattering, at the

360 10s of kilometers scale, there is significant variability in the amplitude (Fig. S3).

361 **4. Discussion: Using Incoherent Scattering in Ice Core Site Selection**

362 There is compelling evidence that incoherent scattering can arise from fabric transitions in the deep ice, and the quality of that

363 scattering could be diagnostic of large-scale deformation that is co-located with the smaller-scale fabric development. If true,

364 then incoherent scattering might be used to improve ice core site selection. We test that theory at 17 ice core sites, by first

365 subdividing core-adjacent radar imagery into five types of signal (Figs. 5a and 5b):

366

367   1. Laterally continuous coherent scattering (that is, clear isochronal layering)

368   2. Diffuse but banded scattering

369   3. Laterally homogenous incoherent scattering

370   4. Laterally heterogeneous incoherent scattering

371   5. No signal (or rather, signal levels at or below the noise floor of the system).

372
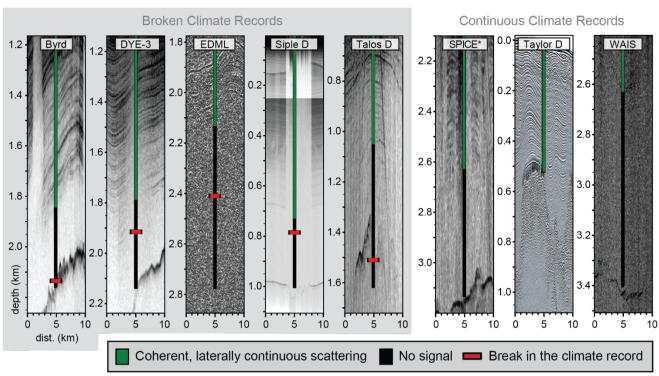
373 We then compare these scattering types to known breaks in the continuity of the associated ice cores (see Appendix A for the

374 observational basis for each labelled break).

375

376 Across these core sites, continuous coherent scattering is almost exclusively found above known breaks in the climate record.

377 This type of scattering appears below the break in a climate record in only one ice core, and that is Vostok, where the interface

between accreted and meteoric ice and a layer of mineral inclusions from the lake bed (Turkeev et al., 2021) define two clear reflection horizons. As a result, in typical glaciological environments, continuous coherent scattering is a robust indicator of ice core continuity. At the studied core sites, where diffuse but banded scattering sits immediately below laterally continuous layering (as is the case at EDC and EastGRIP), there are no associated breaks in measured climate records. This supports the idea that banded but incoherent scattering is not an indication of disturbed basal ice.
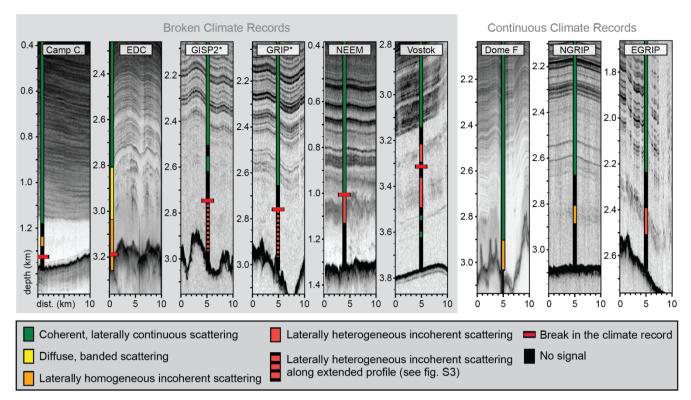
Where we see laterally homogenous incoherent scattering, as in Camp Century, EDC, Dome Fuji, and NorthGRIP, it occurs within sections of ice with a continuous climate record. This likely indicates fabric transitions that are themselves defined weakly by depositional impurities, and thus, the shape of the scattering band is roughly parallel to the isochronous layering. At Vostok, we see incoherent scattering that is laterally heterogeneous in its intensity but is otherwise layering conformal, directly above and ~100 - 200 m below the broken climate record. These two bands of incoherent scattering are qualitatively indistinguishable, and demonstrate the challenge of interpreting the quality of the climate record within regions characterized by bed conformal laterally heterogeneous incoherent scattering.

But where we see laterally heterogeneous incoherent scattering that is layering non-conformal (as in GISP2, GRIP, and NEEM) it occurs below breaks in the continuity of the observed climate record. We show that the source of the backscattering is transition in the crystal fabric of the glacier, and its macro-scale expression comes from the nature of the vertical and lateral heterogeneity in fabric. In those places, it is possible that the same ice rheology contrast that facilitated a fabric transition interacts with the complex, local, basal stress regime to enable multi-meter scale deformation. This induces lateral variability in the backscatter intensity, and can be taken as a significant risk for a disturbed climate record.

*SPICECore drilling ceased at 1500 m. The continuity of the climate record below 1500 m is unknown.

Figure 5a

399

400

Figure 5b

Figure 5: 10 km length radar profiles collected proximal to the 17 ice core drill sites. Radargrams are 1100 m in depth, spanning the bottom 1000 m of each ice core. Backscatter power color scales are standardized to span 0.5% to 99% of the return power amplitude recorded in the presented depth range (except for Taylor Dome where the raw data has been lost). Radar system characteristics can be found in Supplementary Table 1. The depth of the broken climate record, described in Appendix A, is marked at the relevant core sites. The quality of radar scattering at the ice core drill site is color-coded based on categorization as coherent, diffuse and banded, incoherent and laterally homogeneous, incoherent and laterally heterogeneous, or no signal (below the noise floor). (a) Radargrams from Byrd, Dye-3, EDML, Siple Dome, Talos Dome, South Pole, Taylor Dome, and WAIS Divide exhibit coherent laterally continuous scattering until the noise floor of the radar instrument, or bedrock at Taylor Dome, is reached. Lack of scattering once the instrument reaches the noise floor inhibits interpretation of the quality of the climate record at depth. (b) Radargrams from Camp Century, EDC, GISP2, GRIP, NEEM, Vostok, Dome Fuji, NorthGRIP, and EastGRIP exhibit a variety of incoherent scattering patterns. Incoherent scattering is observed within both continuous climate records at Camp Century, EDC, Vostok, Dome Fuji, NorthGRIP, and EastGRIP, and broken climate records at EDC, GRIP, GISP2, NEEM, Vostok. *Laterally heterogeneous incoherent scattering at GISP2 and GRIP is best observed along the extended 35 km radar transects in Fig. S3.

5. Conclusions

Based on comparison between ice core data and ice-penetrating radar imagery at ice core sites, we show that diffuse and incoherent scattering is often collocated with transitions in the crystal orientation fabric of the ice. Transitions in fabric are a product of the local stress regime, but they are localized by differences in grain size. High concentrations of impurities tend to reduce local grain-size and enhance deformation rates, so where climatically driven variations in impurities change the strength

of the ice, one might also expect more abrupt contrasts in fabric that back-scatter radio waves. In this way, fabric controlled scattering may be roughly isochronous, although we show that fabric interfaces do not manifest as abrupt, specular reflectors the way chemically induced layering does in radar imagery.

In the deep ice, where stresses are high, the age-depth scale is compressed, and global changes in impurity deposition are expressed over narrower depth ranges, we might expect fabric induced scattering to be common. The nature of the fabric transition, and the spatial heterogeneity in the transition, define whether or not the scattering will appear as coherent layering, a diffuse scattering horizon, laterally homogenous incoherent scattering, or laterally heterogeneous incoherent scattering. In addition, ice fluidity contrasts at fabric boundaries facilitate small- and large-scale folding. At small scales (below ~1 m), folding seems to have little impact on existing radar data. But large-scale folding, where present, results in complex scattering targets in the subsurface, and induces significant lateral heterogeneity in the incoherent scattering intensity and complex scattering horizons. Where this is observed at existing ice core sites, it seems indicative of discontinuities in the ice core climate record.

A final consideration when thinking about fabric induced incoherent scattering is the relationship between permittivity contrasts (as experienced by the propagating radio-wave) and radio-wave polarization. For fabric intensification (for example, a weak single maximum to a strong single maximum fabric) there will be a change in permittivity for all radar polarizations, and scattering will likely appear isotropic. For fabric transitions (for example, from a girdle to a single maximum fabric) it is possible for some polarizations to exhibit scattering and others to have low backscatter or apparent echo free zones. This anisotropic character merits further study at places like Siple Dome, EDML, EastGRIP, and Vostok, where girdles are seen in the deep ice.

As is true for discussions of the "echo free zone", we show that conversations about the "basal layer" observed in Greenland and Antarctica must start from the understanding that deep scattering (or its absence) depends on system characteristics and physical properties of the ice. Both echo free zones and deep incoherent scattering could arise from multiple mechanisms. We show that a common mechanism for incoherent scattering in deep ice is transition in ice crystal fabric. We find that qualitative differences in the nature of incoherent scattering can aid in evaluating the suitability of future ice core sites. But most importantly, we hope to emphasize that incoherent scattering is signal, not noise, and more work should be done to better interpret this often overlooked component of radar imagery.

6. Data Availability

The radar data and associated metadata used in this analysis is available in the accompanying data dictionary (https://doi.org/10.7910/DVN/JAQJWZ).

7. Author Contribution

EM synthesized data from the literature on physical and chemical properties of ice cores and identified radar data from CReSIS, BAS, UT, UW, and AWI. All authors contributed to study design, radargram interpretation, figure creation, and writing of manuscript.

8. Competing Interests

The authors declare that they have no conflict of interest.

9. Acknowledgements

This work was funded through the Center for Oldest Ice Exploration (NSF-2019719). It also represents an aggregation of a tremendous amount of work from previous scholars studying ice cores, and we would like to thank those communities and encourage suggestions from those scholars for new ways to connect ice penetrating radar to measurable ice core quantities.

Appendix A. Known Layer Disturbances and Ice Core Continuity Problems

Of the cores studied, 6 show only minor signs of layer disturbances, and contain a continuous climate record through the full depth range of the ice core. Those are EastGRIP, Dome Fuji, NorthGRIP, SPICEcore, Taylor Dome, and WAIS Divide. Of the other 11 cores, 6 have well identified breaks in their climate record, and 4 are likely discontinuous (although the exact stratigraphic break is not well identified), and 1 has conflicting observations of discontinuity. Here, we describe the observational basis for claims of a broken climate record.

A.1 Cores with Clear Evidence of Stratigraphic Discontinuities

(Alphabetically: EDML, GRIP, GISP2, NEEM, Talos Dome, Vostok)

EPICA (European Project for Ice Coring in Antarctica) Dronning Maud Land, EDML (Length: 2774 m | Break: 2417 m | Percentage Disturbed: 12.9%): The chronology called EDML1 has been established for the top 2417 m of the EDML ice core. The top 2366 m of the core is matched to the EDC3 chronology using volcanic signatures (dielectric profiling (DEP), SO_4 concentrations, and electrolyte conductivity measurements) (Ruth et al., 2007). Three tie points between the EDC3 chronology and EDML core are matched between 2366 and 2415 m using insoluble dust concentrations, $\delta^{18}O$, and δD, however these matches are considered uncertain with estimated errors up to several thousand years (Ruth et al., 2007). Macrostructure analysis of linescan images between 2400 and 2500 m shows evidence of large-scale folding (Faria et al., 2010).

Greenland Ice Core Project, GRIP (Length: 3029 m | Break: ~2750 m | Percentage Disturbed: 9.2%) and Greenland Ice Sheet Project Two, GISP2D (Length: 3053.4 m | Break: ~2750 m | Percentage Disturbed: 9.9%): CH_4 and $\delta^{18}O_{atm}$ data from both GRIP and GISP2 show evidence of stratigraphic disturbance in the bottom 10% the ice cores. Above 2750 m CH_4 and $\delta^{18}O_{atm}$ values vary synchronously between GRIP and GISP2, but below 2750 m, the chemical profiles diverge, showing large and significant fluctuations which are not present in the undisturbed ice from the Vostok 3G core (Chappellaz et al., 1997).

North Greenland Eemian Ice Drilling, NEEM (Length: 2540 m | Break: 2209.6 m | Percentage Disturbed: 13%): At NEEM, an abrupt discontinuity in the $\delta^{18}O_{ice}$ at 2209.6 m marks the end of synchronization with the NorthGRIP GICC05 extended timescale. Additional discontinuities in the $\delta^{18}O_{ice}$ subdivide the bottom 13% of the core into six zones of disturbed stratigraphy. These correspond with similar shifts in other atmospheric gas measurements (CH_4, $\delta^{18}O_{atm}$, N_2O, $\delta^{15}N$ of N_2). Within the upper five zones, the layering is thought to be unbroken (based on continuous records of N_2O, $\delta^{15}N$ of N_2, dust, or electrical properties), with timescales for each of the upper five zones reconstructed by synchronizing NEEM $\delta^{18}O_{atm}$ and CH_4 profiles with NorthGRIP and EDML records. The timescales for these zones include inverted, mirrored, and folded ice up to 100 m thick (NEEM Community Members, 2013).

496

TALos Dome Ice CorE, TALDICE (Length: 1620 m | Break: 1548 m | Percentage Disturbed: 4.4%): At Talos Dome, Crotti et al. identify a break in stratigraphic continuity at 1548 m using analysis of $\delta^{18}O_{atm}$, δD, and 81Kr dating, described below (Crotti et al., 2021). TALDICE $\delta^{18}O_{atm}$ and δD measurements were matched to the EDC $\delta^{18}O_{atm}$ and δD record through visual synchronization through 1548 m depth. Below 1548 m, the amplitude of $\delta^{18}O_{atm}$ fluctuations is damped, making synchronization with the EDC record uncertain. Similarly, below 1548 m, the TALDICE δD signal becomes asynchronous with the EDC record. [81]Kr dating of three samples below 1548 m depth revealed that ice from 1613 - 1618 m had comparable age to samples from 1559 - 1563 m and 1573 - 1578 m depth, indicating a disturbed age-depth relationship.

Vostok 5G-5 (Length: 3658 m | Break: 3311 m | Percentage Disturbed: 9.5%): The stratigraphy in the bottom 9% of the Vostok 5G core is divided between 228 m of disturbed meteoric ice, and 119 m of accreted lake ice. In the upper part of the disturbed meteoric ice, the lack of depth-shift between δD_{ice} and gas measurements (CO_2 and CH_4) is interpreted by Souchez et al. as evidence of folding and intermixing (Souchez et al., 2002). Observations of ash layers with depth-varying inclinations supports interpretation of large-scale folding. In the lower part of the disturbed meteoric ice, damped variation of δD_{ice} and trace impurity distributions (Na+, Cl-, non-sea salt Mg++ and Ca++), physical observations of interbedded fine-grained (presumably glacial) and coarse-grained (presumably interglacial) ice, and the presence of bed material in the bottom 100 m of the disturbed meteoric ice, is interpreted as further evidence for stratigraphic deformation (Lipenkov and Raynaud, 2015; Souchez et al., 2002). At 3538 m depth, the transition between meteoric and accreted ice is apparent from the $\delta D_{ice}/ \delta^{18}O$ fingerprint of freezing processes (Jouzel et al., 1999). At this depth, sudden transitions to lower total gas content, increased crystal size, low ECM values, increased δD_{ice}, and decreased deuterium excess, provide further evidence for the meteoric/accreted ice transition (Jouzel et al., 1999).

A.2 Cores that Likely Contain Stratigraphic Discontinuities or Conflicting Observations of Discontinuity

(Alphabetically: Byrd, Camp Century, EPICA Dome C, Dye-3, Siple Dome)

Byrd Station '68, BYRD 68 (Length: 2164 m | Break: 2135-2144 m | Percentage Disturbed: ~1%): A chronology for the upper ~99% (2144 m) of the Byrd core has been established by synchronizing Byrd, GRIP, and GISP2 CH_4 profiles (Blunier and Brook, 2001). Gas volume measurements from the bottom 10 m of the core (2154 - 2164 m) suddenly approach zero at 4.83 m above the bed, revealing the transition between meteoric ice and accreted subglacial meltwater (Gow et al., 1979). The bottom 4.83 m of non-meteoric ice contain horizontal bands of basal debris including sand, clay, and pebbles as large as 8 cm in diameter (Gow et al., 1979). Grootes et al. 2001 observe that the Byrd $\delta^{18}O$ record becomes asynchronous with Taylor Dome and Vostok record around 2135 m.

Camp Century, CC 63-66 (Length: 1387.4 m | Break: ~1350 m | Percentage Disturbed: 2.7%): The integrity of the Camp Century climate record is uncertain below 1310 m depth where $\delta^{18}O$ profiles of Camp Century, GRIP, and GISP2 become asynchronous (Johnsen et al., 2001). Correlation of a smoothed Camp Century $\delta^{18}O$ profile with benthic foraminifera record from deep sea core RC11-120 provides a tentative extension of the chronology through about 1330 m, the depth of the inflection point associated with Marine Isotope Stage (MIS) 5d (Dansgaard et al., 1985). A dramatic cold event at 1340 m is associated with a similar $\delta^{18}O$ fluctuation in the disturbed section of the GRIP core at 2800 m (Johnsen et al., 2001). Johnsen et al. describe dramatic fluctuations in $\delta^{18}O$ below Greenland Interstadial (GI) 23 in the GRIP, GISP2, and Camp Century cores which are not represented in the continuous $\delta^{18}O$ signal from Vostok (Chappellaz et al., 1997).

EPICA Dome C, EDC99 (Length: 3260 m | Potential Break: ~3200 m | Percentage Disturbed: ~1.8%): The continuity of the upper 98% (3200 m) of the EDC99 core is evidenced primarily through matching of δD_{ice} to the deep-sea benthic $\delta^{18}O$ record (Jouzel et al., 2007). Additional matching of enhanced [10]Be deposition to Matuyama-Brunhes geomagnetic reversal between 3160 and 3170 m (Jouzel et al., 2007) and matching of CO_2 and CH_4 profiles to MIS18 and 19 between 3160 and 3185 m further support the continuity of the upper 98% of the core. Below 3200 m, there is contradictory evidence about the continuity of the climate record. Measurements of δD, total air content, gas composition, and dust content suggest continuity to bedrock, while $\delta^{18}O_{atm}$, visible inclusions, length of the glacial period, and variability of chemical species distribution suggest altered stratigraphy (Tison et al., 2015).

DYE-3, DYE3 79-81 (Length: 2037 m | Break: 1940 m | Percentage Disturbed: 4.8%): At DYE-3, the continuity of the climate signal is lost between 1900 and 1987 m. Initially, Dansgaard et al. 1982 correlated fluctuations between the $\delta^{18}O$ measurements at DYE-3 and Camp Century through 1987 m depth. Between 1987 and 2010 m, DYE-3 $\delta^{18}O$ values are quasi-constant, and interpreted as evidence of folded layers. Later, comparison of the $\delta^{18}O$ values between DYE-3 and GRIP led Johnsen et al., 2001 to identify Greenland Interstadial (GI) 8 at 1900 m as the last undisturbed match point between the two records. However, Johnsen et al. would still identify two match points in the deeper ice: GI 12 (~1925 m) and GI 14 (~1940 m). Recent analysis of $\delta^{15}N$-N_2 and CH_4 gas records may suggest stratigraphic disturbance beginning at 1895 m depth (Buizert et al., 2024). Since the scale of the gas record disturbances has not yet been quantified, in our analysis we have used 1940 m as the depth of the broken climate record. CO_2 and CH_4 measurements of the bottom 27 m of silty ice have been used to identify 4 distinct zones of highly deformed basal ice (Verbeke et al., 2002).

Siple Dome A, SDMA (Length: 1004 m | Break: ~800 m | Percentage Disturbed: ~20%): The integrity of the Siple Dome climate record is uncertain in the bottom 200 m of the core, however a precise onset depth for the disturbed ice is poorly constrained. A chronology for the 514 - 854 m section of the core was established by synchronizing Siple Dome, GISP2, and GRIP CH_4 profiles (Brook et al., 2005). Below 854 m, the methane data becomes sparse however a possible chronology has been proposed between 854 and 920 m based on the matching of a single inflection point in the $\delta^{18}O_{atm}$ profile of Siple Dome

core at 920 m with a corresponding GISP2 $\delta^{18}O_{atm}$ inflection point (Brook et al., 2005). Macro and micro-scale physical observations by Gow and Meese suggest an interrupted climate record by 800 m depth, summarized here (Gow and Meese, 2007). Between 560 and 800 m, sequences of inclined layering occasionally surpassing 10 degrees as well as reversed dips are observed. Below 800 m the core is highly fractured, limiting any further observations of layer structure. Around 700 m, the c-axis fabric shifts suddenly to a single maximum corresponding to a stress regime dominated by strong horizontal shear. Around 800 m, the c-axis fabric shifts back to a multi-maxima fabric.

A.3 Cores with No Significant Break in Continuity

(Alphabetically: EastGRIP, Dome Fuji, NorthGRIP, SPICEcore, Taylor Dome, WAIS Divide)

East Greenland Ice Core Project, EastGRIP (Length: 2663 m): Initial assessment of the continuity of the EastGRIP climate record has been performed through synchronization of DEPs and ECMs to NEEM and NGRIP datasets. These techniques have been used to establish the GICC05-EGRIP-1 timescale for the upper 1383.4 m of the core (Mojtabavi et al., 2020). Preliminary comparison of EastGRIP and NGRIP DEP data from the bottom 260 m of the core have been used to construct rough GI tie points through GI 25a (around 2590 m) as well as evidence of the Eemian-Glacial transition at 2618 m (Stoll et al., 2024). Observations of cm-scale overturning folds, boudin-like structures, and inclined layers with opposing tilts are observed periodically between 1375 and 2121 m, the depth of the deepest linescan image (Westhoff, 2021; Weikusat, 2020). Due to the rough synchronization of DEP data below the depths of the linescan images, these physical observations of cm-scale disturbances are not interpreted as significant breaks in the climate record.

Dome Fuji, DF2 (Length: 3035.22 m): The integrity of the Dome Fuji ice core climate record is discussed by the (Dome Fuji Ice Core Project Members, 2017) and summarized here. A chronology for the upper 3028 m of the 3035 m Dome Fuji core was established through the synchronization of $\delta^{18}O$ records to the EDC δD profile. Physical observations of inclined layers begin at 2400 m and show distinct stepwise increases in inclination: ~8° between 2450 - 2600, ~20° between 2600 - 2800, ~40° between 2800 - 2900, ~45° at 2950 m, and ~50° at bedrock. Despite the observations of inclined layers, which are attributed to spatially variable basal melt conditions, explicit observations of folded layers were not noted and the synchroneity of the $\delta^{18}O$ and EDC δD profiles are considered evidence of an intact climate record within the depths of inclined layers.

North Greenland Ice Core Project, NorthGRIP2 (Length: 3090 m): At NorthGRIP, the continuity of the 2544 – 3073 m zone of the 3090 m length core was confirmed by matching NorthGRIP $\delta^{18}O_{atm}$ and CH_4 records to EDML and EDML1 chronologies (Capron et al., 2010). Depth shift analysis at 2940 m showed the expected shift between $\delta^{15}N$ and CH_4 vs $\delta^{18}O$ during Dansgaard-Oescher (DO) 24, and was used to confirm the continuity of the deepest layers (North Greenland Ice Core Project Members, 2004). Like at WAIS Divide, small scale stratigraphic disturbances are observed a few hundred meters above bedrock (Svensson, 2005), but are not considered large enough to impact the continuity of the climate record.

South Pole Ice Core, SPICEcore, SPC14 (Length: 1500 m | Ice thickness: 2700 m): Continuity through the end of the core is established through synchronization of CH_4 fluctuations to WAIS Divide ice core (Epifanio et al., 2020). Notably, SPICEcore drilling stopped 1200 m above bedrock.

Taylor Dome, M3C1 (Length: 554 m): The continuity of the Taylor Dome core was established through correlation of the CH_4 and $\delta^{18}O_{atm}$ profiles with corresponding GISP2 profiles as well as correlation of the $\delta^{18}O$ profile with the Vostok δD record (Grootes et al., 2001; Steig et al., 1998). The $\delta^{18}O$ inflection point associated with MIS 5e (~130kyrBP) is identified between 526 and 531 m depth. The identification of correlated inflection points continues confidently through 200 kyrBP with a tentative chronology, limited by sample resolution, extending beyond 300 kyrBP (Grootes et al., 2001).

WAIS (West Antarctic Ice Sheet) Divide, WDC06A (Length: 3405 m | Ice thickness: 3455 m): The continuity of the WAIS Divide core is confirmed above 2850 m by annual layer counting, and below 2850 m via synchronization of WAIS Divide CH_4 measurements to the NorthGRIP $\delta^{18}O$ record and a refined Hulu Cave speleothem $\delta^{18}O$ record (Buizert et al., 2015). Notably, the 3405 m WAIS Divide core ends 50 m above bedrock, so continuity in the uncored 50 m basal unit is not confirmed. Mm-scale or smaller stratigraphic disturbances are observed at 3150 and 3232 m (Fitzpatrick et al., 2014) but are not considered large enough to impact the continuity of the climate record.

References

Alley, R. B., Gow, A. J., Johnsen, S. J., Kipfstuhl, J., Meese, D. A., and Thorsteinsson, T.: Comparison of deep ice cores, Nature, 373, 393–394, https://doi.org/10.1038/373393b0, 1995.

Alley, R. B., Gow, A. J., Meese, D. A., Fitzpatrick, J. J., Waddington, E. D., and Bolzan, J. F.: Grain-scale processes, folding, and stratigraphic disturbance in the GISP2 ice core, J. Geophys. Res. Oceans, 102, 26819–26830, https://doi.org/10.1029/96JC03836, 1997.

Azuma, N., Wang, Y., Mori, K., Narita, H., Hondoh, T., Shoji, H., and Watanabe, O.: Textures and fabrics in the Dome F (Antarctica) ice core, Ann. Glaciol., 29, 163–168, https://doi.org/10.3189/172756499781821148, 1999.

Bingham, R. G., Bodart, J. A., Cavitte, M. G. P., Chung, A., Sanderson, R. J., Sutter, J. C. R., Eisen, O., Karlsson, N. B., MacGregor, J. A., Ross, N., Young, D. A., Ashmore, D. W., Born, A., Chu, W., Cui, X., Drews, R., Franke, S., Goel, V., Goodge, J. W., Henry, A. C. J., Hermant, A., Hills, B. H., Holschuh, N., Koutnik, M. R., Leysinger Vieli, G. J.-M. C., Mackie, E. J., Mantelli, E., Martín, C., Ng, F. S. L., Oraschewski, F. M., Napoleoni, F., Parrenin, F., Popov, S. V., Rieckh, T., Schlegel, R., Schroeder, D. M., Siegert, M. J., Tang, X., Teisberg, T. O., Winter, K., Yan, S., Davis, H., Dow, C. F., Fudge, T. J., Jordan, T. A., Kulessa, B., Matsuoka, K., Nyqvist, C. J., Rahnemoonfar, M., Siegfried, M. R., Singh, S., Višnjević, V., Zamora, R., and Zuhr, A.: Review Article: Antarctica's internal architecture: Towards a radiostratigraphically-informed age–depth model of the Antarctic ice sheets, EGUsphere [preprint], https://doi.org/10.5194/egusphere-2024-2593, 1 October 2024.

Blunier, T. and Brook, E. J.: Timing of millennial-scale climate change in Antarctica and Greenland during the Last Glacial Period, Science, 291, 109–112, https://doi.org/10.1126/science.291.5501.109, 2001.

Brook, E. J., White, J. W. C., Schilla, A. S. M., Bender, M. L., Barnett, B., Severinghaus, J. P., Taylor, K. C., Alley, R. B., and Steig, E. J.: Timing of millennial-scale climate change at Siple Dome, West Antarctica, during the last glacial period, Quat. Sci. Rev., 24, 1333–1343, https://doi.org/10.1016/j.quascirev.2005.02.002, 2005.

Buizert, C., Cuffey, K. M., Severinghaus, J. P., Baggenstos, D., Fudge, T. J., Steig, E. J., Markle, B. R., Winstrup, M., Rhodes, R. H., Brook, E. J., Sowers, T. A., Clow, G. D., Cheng, H., Edwards, R. L., Sigl, M., McConnell, J. R., and Taylor, K. C.: The WAIS Divide deep ice core WD2014 chronology – Part 1: Methane synchronization (68–31 ka BP) and the gas age–ice age difference, Clim. Past, 11, 153–173, https://doi.org/10.5194/cp-11-153-2015, 2015.

Capron, E., Landais, A., Lemieux-Dudon, B., Schilt, A., Masson-Delmotte, V., Buiron, D., Chappellaz, J., Dahl-Jensen, D., Johnsen, S., Leuenberger, M., Loulergue, L., and Oerter, H.: Synchronising EDML and NorthGRIP ice cores using $\delta^{18}O$ of atmospheric oxygen ($\delta^{18}O_{atm}$) and CH_4 measurements over MIS5 (80–123 kyr), Quat. Sci. Rev., 29, 222–234, https://doi.org/10.1016/j.quascirev.2009.07.014, 2010.

Catania, G. A., Conway, H. B., Gades, A. M., Raymond, C. F., and Engelhardt, H.: Bed reflectivity beneath inactive ice streams in West Antarctica, Ann. Glaciol., 36, 287-291, https://doi.org/10.3189/172756403781816310, 2003.

Chappellaz, J., Brook, E., Blunier, T., and Malaizé, B.: CH_4 and $\delta^{18}O$ of O_2 records from Antarctic and Greenland ice: a clue for stratigraphic disturbance in the bottom part of the Greenland Ice Core Project and the Greenland Ice Sheet Project 2 ice cores, J. Geophys. Res., 102, 26547–26557, https://doi.org/10.1029/97JC00164, 1997.

Christianson, K., Jacobel, R. W., Horgan, H. J., Alley, R. B., Anandakrishnan, S., Holland, D. M., and DallaSanta, K. J.: Basal conditions at the grounding zone of Whillans Ice Stream, West Antarctica, from ice-penetrating radar, J. Geophy. Res. Earth, 121, 1954-1983, https://doi.org/10.1002/2015JF003806, 2016.

Chu. W., Schroeder, D. M., Seroussi, H., Creyts, T. T., and Bell, R. E.: Complex basal thermal transition near the onset of Petermann Glacier, Greenland, J. Geophy. Res. Earth, 123, 985-995, https://doi.org/10.1029/2017JF004561, 2018.

Chung, A., Parrenin, F., Steinhage, D., Mulvaney, R., Martin, C., Cavitte, M. G. P., Lilien, D. A., Veit, H., Taylor, D., Gogineni, P., Ritz, C., Frezzotti, M., O'Neill, C., Heinrich, M., Dahl-Jensen, D., and Eisen, O.: Stagnant ice and age modelling in the Dome C region, Antarctica, The Cryosphere, 17, 3461–3483, https://doi.org/10.5194/tc-17-3461-2023, 2023.

Crotti, I., Landais, A., Stenni, B., Bazin, L., Parrenin, F., Frezzotti, M., Ritterbusch, F., Lu, Z.-T., Jiang, W., Yang, G.-M., Fourré, E., Orsi, A., Jacob, R., Minster, B., Prié, F., Dreossi, G., and Barbante, C.: An extension of the TALDICE ice core age scale reaching back to MIS 10.1, Quat. Sci. Rev., 266, 107078, https://doi.org/10.1016/j.quascirev.2021.107078, 2021.

Dahl-Jensen, D., Gundestrup, N. S., Keller, K., Johnsen, S. J., Gogineni, S. P., Allen, C. T., Chuah, T. S., Miller, H., Kipfstuhl, S., and Waddington, E. D.: A search in North Greenland for a new ice-core drill site, J. Glaciol., 43, 300–306, https://doi.org/10.3189/S0022143000003245, 1997.

Dansgaard, W.: A New Greenland Deep Ice Core, Science, 218, 1273–1277, 1982.

Dansgaard, W., Clausen, H. B., Gundestrup, N., Johnsen, S. J., and Rygner, C.: Dating and climatic interpretation of two deep Greenland ice cores, in: Greenland Ice Core: Geophysics, Geochemistry, and the Environment, vol. 33, edited by: Langway, C. C., Oeschger, H., and Dansgaard, W., American Geophysical Union, Washington, D. C., 71–76, https://doi.org/10.1029/GM033p0071, 1985.

Dome Fuji Ice Core Project Members: State dependence of climatic instability over the past 720,000 years from Antarctic ice cores and climate modeling, Sci. Adv., 3, https://doi.org/10.1126/sciadv.1600446, 2017.

Dowdeswell, J. A. and Evans, S.: Investigations of the form and flow of ice sheets and glaciers using radio-echo sounding, Rep. Prog. Phys., 67, 1821–1861, https://doi.org/10.1088/0034-4885/67/10/R03, 2004.

Durand, G., Svensson, A., Persson, A., Gillct-Chaulc, F., Montagnat, M., and Dahl-Jensen, D.: Evolution of the texture along the EPICA Dome C ice core, Physics of Ice Core Records II : Papers collected after the 2nd International Workshop on Physics of Ice Core Records, held in Sapporo, Japan, 68, 91–105, 2009.

Eichler, J.: C-axis analysis of the NEEM ice core, Master's Thesis, Freie Universitat, Berlin, Germany, 63 pp., 2013.

Eisen, O., Wilhelms, F., Nixdorf, U., and Miller, H.: Revealing the nature of radar reflections in ice: DEP-based FDTD forward modeling, Geophys. Res. Lett., 30, https://doi.org/10.1029/2002GL016403, 2003.

Eisen, O., Hamann, I., Kipfstuhl, S., Steinhage, D., and Wilhelms, F.: Direct evidence for continuous radar reflector originating from changes in crystal-orientation fabric, The Cryosphere, 1, 1–10, https://doi.org/10.5194/tc-1-1-2007, 2007.

Epifanio, J. A., Brook, E. J., Buizert, C., Edwards, J. S., Sowers, T. A., Kahle, E. C., Severinghaus, J. P., Steig, E. J., Winski, D. A., Osterberg, E. C., Fudge, T. J., Aydin, M., Hood, E., Kalk, M., Kreutz, K. J., Ferris, D. G., and Kennedy, J. A.: The SP19 chronology for the South Pole Ice Core – Part 2: gas chronology, Δage, and smoothing of atmospheric records, Clim. Past, 16, 2431–2444, https://doi.org/10.5194/cp-16-2431-2020, 2020.

Fahnestock, M., Abdalati, W., Joughin, I., Brozena, J., and Gogineni, P.: High geothermal heat flow, basal melt, and the origin of rapid ice flow in Central Greenland, Science, 294, 2338–2342, https://doi.org/10.1126/science.1065370, 2001.

Faria, S. H., Freitag, J., and Kipfstuhl, S.: Polar ice structure and the integrity of ice-core paleoclimate records, Quat. Sci. Rev., 29, 338–351, https://doi.org/10.1016/j.quascirev.2009.10.016, 2010.

Faria, S. H., Weikusat, I., and Azuma, N.: The microstructure of polar ice. Part I: Highlights from ice core research, J. Struct. Geol., 61, 2–20, https://doi.org/10.1016/j.jsg.2013.09.010, 2014.

Faria, S. H., Kipfstuhl, S., and Lambrecht, A.: The EPICA-DML Deep Ice Core: A Visual Record, Springer Berlin Heidelberg, Berlin, Heidelberg, 305 pp., https://doi.org/10.1007/978-3-662-55308-4, 2018.

Fegyveresi, J. M. and Alley, R. B.: South Pole Ice Core (SPIcecore) Visual Observations [data set], https://doi.org/10.15784/601088, 2018.

Fitzpatrick, J. J., Voigt, D. E., Fegyveresi, J. M., Stevens, N. T., Spencer, M. K., Cole-Dai, J., Alley, R. B., Jardine, G. E., Cravens, E. D., Wilen, L. A., Fudge, T. J., and Mcconnell, J. R.: Physical properties of the WAIS Divide ice core, J. Glaciol., 60, 1181–1198, https://doi.org/10.3189/2014JoG14J100, 2014.

Fudge, T. J., Taylor, K. C., Waddington, E. D., Fitzpatrick, J. J., and Conway, H.: Electrical stratigraphy of the WAIS Divide ice core: identification of centimeter-scale irregular layering, J. Geophys. Res. Earth Surf., 121, 1218–1229, https://doi.org/10.1002/2016JF003845, 2016.

Fudge, T. J., Hills, B. H., Horlings, A. N., Holschuh, N., Christian, J. E., Davidge, L., Hoffman, A., O'Connor, G. K., Christianson, K., and Steig, E. J.: A site for deep ice coring at West Hercules Dome: results from ground-based geophysics and modeling, J. Glaciol., 69, 538–550, https://doi.org/10.1017/jog.2022.80, 2023.

Fujita, S., Maeno, H., Uratsuka, S., Furukawa, T., Mae, S., Fujii, Y., and Watanabe, O.: Nature of radio echo layering in the Antarctic Ice Sheet detected by a two-frequency experiment, J. Geophys. Res., 104, 13013–13024, https://doi.org/10.1029/1999JB900034, 1999.

Gerber, T. A., Lilien, D. A., Nymand, N. F., Steinhage, D., Eisen, O., and Dahl-Jensen, D.: Anisotropic scattering in radio-echo sounding: insights from Northeast Greenland, EGUsphere [preprint], https://doi.org/10.5194/egusphere-2024-2276, 6 September 2024.

Gow, A. J. and Meese, D.: Physical properties, crystalline textures and c-axis fabrics of the Siple Dome (Antarctica) ice core, J. Glaciol., 53, 573–584, https://doi.org/10.3189/002214307784409252, 2007.

Gow, A. J., Epstein, S., and Sheehy, W.: On the origin of stratified debris in ice cores from the bottom of the Antarctic Ice Sheet, J. Glaciol., 23, 185–192, https://doi.org/10.3189/S0022143000029828, 1979.

Gow, A. J., Meese, D. A., Alley, R. B., Fitzpatrick, J. J., Anandakrishnan, S., Woods, G. A., and Elder, B. C.: Physical and structural properties of the Greenland Ice Sheet Project 2 ice core: a review, J. Geophys. Res., 102, 26559–26575, https://doi.org/10.1029/97JC00165, 1997.

Grootes, P. M., Steig, E. J., Stuiver, M., Waddington, E. D., Morse, D. L., and Nadeau, M.-J.: The Taylor Dome Antarctic [18]O record and globally synchronous changes in climate, Quat. Res., 56, 289–298, https://doi.org/10.1006/qres.2001.2276, 2001.

Hammer, C. U.: Acidity of polar ice cores in relation to absolute dating, past volcanism, and radio echoes, J. Glaciol., 24, 359-372, https://doi.org/10.3189/S0022143000015227, 1980.

Hamran, S., Aarholt, E., Hagen, J. O., and Mo, P.: Estimation of relative water content in a sub-polar glacier using surface-penetration radar, J. Glaciol., 42, 533–537, 1996.

Harrison, C. H.: Radio echo sounding of horizontal layers in ice, J. Glaciol., 12, 383-397, https://doi.org/10.3189/S0022143000031804, 1973.

Howat, I. M., Porter, C., Smith, B. E., Noh, M.-J., and Morin, P.: The reference elevation model of Antarctica, The Cryosphere, 13, 665–674, https://doi.org/10.5194/tc-13-665-2019, 2019.

Jansen, D., Llorens, M.-G., Westhoff, J., Steinbach, F., Kipfstuhl, S., Bons, P., Griera, A., and Weikusat, I.: Small-scale disturbances in the stratigraphy of the NEEM ice core: observations and numerical model simulations, The Cryosphere Discussions, 9, https://doi.org/10.5194/tcd-9-5817-2015, 2015.

Johnsen, S. J., Clausen, H. B., Dansgaard, W., Gundestrup, N. S., Hammer, C. U., and Tauber, H.: The Eem stable isotope record along the GRIP ice core and its interpretation, Quat. Res., 43, 117–124, https://doi.org/10.1006/qres.1995.1013, 1995.

Johnsen, S. J., Dahl-Jensen, D., Gundestrup, N., Steffensen, J. P., Clausen, H. B., Miller, H., Masson-Delmotte, V., Sveinbjörnsdottir, A. E., and White, J.: Oxygen isotope and palaeotemperature records from six Greenland ice-core stations: Camp Century, Dye-3, GRIP, GISP2, Renland and NorthGRIP, J. Quat. Sci., 16, 299–307, https://doi.org/10.1002/jqs.622, 2001.

Jouzel, J. and Masson-Delmotte, V.: Deep ice cores: the need for going back in time, Quat. Sci. Rev., 29, 3683–3689, https://doi.org/10.1016/j.quascirev.2010.10.002, 2010.

Jouzel, J., Petit, J. R., Souchez, R., Barkov, N. I., Lipenkov, V. Ya., Raynaud, D., Stievenard, M., Vassiliev, N. I., Verbeke, V., and Vimeux, F.: More than 200 meters of lake ice above subglacial Lake Vostok, Antarctica, Science, 286, 2138–2141, https://doi.org/10.1126/science.286.5447.2138, 1999.

Jouzel, J., Masson-Delmotte, V., Cattani, O., Dreyfus, G., Falourd, S., Hoffmann, G., Minster, B., Nouet, J., Barnola, J. M., Chappellaz, J., Fischer, H., Gallet, J. C., Johnsen, S., Leuenberger, M., Loulergue, L., Luethi, D., Oerter, H., Parrenin, F., Raisbeck, G., Raynaud, D., Schilt, A., Schwander, J., Selmo, E., Souchez, R., Spahni, R., Stauffer, B., Steffensen, J. P., Stenni, B., Stocker, T. F., Tison, J. L., Werner, M., and Wolff, E. W.: Orbital and millennial Antarctic climate variability over the past 800,000 years, Science, 317, 793–796, https://doi.org/10.1126/science.1141038, 2007.

Karlsson, N. B., Binder, T., Eagles, G., Helm, V., Pattyn, F., Liefferinge, B. V., and Eisen, O.: Glaciological characteristics in the Dome Fuji region and new assessment for oldest ice, The Cryosphere, 12, 2413–2424, https://doi.org/10.5194/tc-12-2413-2018, 2018.

Karlsson, N. B., Razik, S., Hörhold, M., Winter, A., Steinhage, D., Binder, T., and Eisen, O.: Surface accumulation in Northern Central Greenland during the last 300 years, Ann. Glaciol., 61, 214–224, https://doi.org/10.1017/aog.2020.30, 2020.

Kipfstuhl, S.: Visual Stratigraphy of the NEEM Ice Core with Linescanner [data set], https://doi.org/10.1594/PANGAEA.743062, 2009.

Kluskiewicz, D., Waddington, E. D., Anandakrishnan, S., Voigt, D. E., Matsuoka, K., and McCarthy, M. P.: Sonic methods for measuring crystal orientation fabric in ice, and results from the West Antarctic Ice Sheet (WAIS) Divide, J. Glaciol., 63, 603–617, https://doi.org/10.1017/jog.2017.20, 2017.

Landais, A., Chappellaz, J., Delmotte, M., Jouzel, J., Blunier, T., Bourg, C., Caillon, N., Cherrier, S., Malaizé, B., Masson-Delmotte, V., Raynaud, D., Schwander, J., and Steffensen, J. P.: A tentative reconstruction of the last interglacial and glacial inception in Greenland based on new gas measurements in the Greenland Ice Core Project (GRIP) ice core, J. Geophys. Res. Atm., 108, https://doi.org/10.1029/2002JD003147, 2003.

Langway, C. C., Shoji, H., and Azuma, N.: Crystal size and orientation patterns in the Wisconsin-age ice from Dye 3, Greenland, Ann. Glaciol., 10, 109–115, https://doi.org/10.3189/S0260305500004262, 1988.

Leysinger Vieli, G. J.-M. C., Hindmarsh, R. C. a, and Siegert, M. J.: Three-dimensional flow influences on radar layer stratigraphy, Ann. Glaciol., 22–28, 2007.

Lilien, D. A., Steinhage, D., Taylor, D., Parrenin, F., Ritz, C., Mulvaney, R., Martín, C., Yan, J.-B., O'Neill, C., Frezzotti, M., Miller, H., Gogineni, P., Dahl-Jensen, D., and Eisen, O.: Brief communication: new radar constraints support presence of ice older than 1.5 Myr at Little Dome C, The Cryosphere, 15, 1881–1888, https://doi.org/10.5194/tc-15-1881-2021, 2021.

Lindzey, L. E., Beem, L. H., Young, D. A., Quartini, E., Blankenship, D. D., Lee, C.-K., Lee, W. S., Lee, J. I., and Lee, J.: Aerogeophysical characterization of an active subglacial lake system in the David Glacier catchment, Antarctica, The Cryosphere, 14, 2217–2233, https://doi.org/10.5194/tc-14-2217-2020, 2020.

Lipenkov, V. Ya. and Raynaud, D.: The Mid-Pleistocene transition and the Vostok oldest ice challenge, Ice and Snow, 55, 95–106, https://doi.org/10.15356/2076-6734-2015-4-95-106, 2015.

Matsuoka, T., Fujita, S., and Mae, S.: Dielectric properties of ice containing ionic impurities at microwave frequencies. J. Phys. Chem. B., 101(32), 6219-6222, https://doi.org/10.1021/jp9631590, 1997.

Millar, D. H. M.: Acidity levels in ice sheets from radio echo-soundings. Ann. Glaciol., 3, 199-203, https://doi.org/10.3189/S0260305500002779, 1982.

Miyamoto, A., Weikusat, I., and Hondoh, T.: Complete determination of ice crystal orientation using Laue X-ray diffraction method, J. Glaciol., 57, 103–110, https://doi.org/10.3189/002214311795306754, 2011.

Mojtabavi, S., Eisen, O., Franke, S., Jansen, D., Steinhage, D., Paden, J., Dahl-Jensen, D., Weikusat, I., Eichler, J., and Wilhelms, F.: Origin of englacial stratigraphy at three deep ice core sites of the Greenland Ice Sheet by synthetic radar modelling, J. Glaciol., 68, 799–811, https://doi.org/10.1017/jog.2021.137, 2022.

Mojtabavi, S., Wilhelms, F., Cook, E., Davies, S. M., Sinnl, G., Skov Jensen, M., Dahl-Jensen, D., Svensson, A., Vinther, B. M., Kipfstuhl, S., Jones, G., Karlsson, N. B., Faria, S. H., Gkinis, V., Kjær, H. A., Erhardt, T., Berben, S. M. P., Nisancioglu, K. H., Koldtoft, I., and Rasmussen, S. O.: A first chronology for the East Greenland Ice-core Project (EGRIP) over the Holocene and last glacial termination, Clim. Past, 16, 2359–2380, https://doi.org/10.5194/cp-16-2359-2020, 2020.

Montagnat, M., Buiron, D., Arnaud, L., Broquet, A., Schlitz, P., Jacob, R., and Kipfstuhl, S.: Measurements and numerical simulation of fabric evolution along the Talos Dome ice core, Antarctica, Earth and Planetary Science Letters, 357–358, 168–178, https://doi.org/10.1016/j.epsl.2012.09.025, 2012.

Montagnat, M., Azuma, N., Dahl-Jensen, D., Eichler, J., Fujita, S., Gillet-Chaulet, F., Kipfstuhl, S., Samyn, D., Svensson, A., and Weikusat, I.: Fabric along the NEEM ice core, Greenland, and its comparison with GRIP and NGRIP ice cores, The Cryosphere, 8, 1129–1138, https://doi.org/10.5194/tc-8-1129-2014, 2014.

Mouginot J., and Rignot E.: Glacier catchments/basins for the Greenland Ice Sheet [data set], Dryad, https://doi.org/10.7280/D1WT11, 2019.

Mulvaney, R., Rix, J., Polfrey, S., Grieman, M., Martìn, C., Nehrbass-Ahles, C., Rowell, I., Tuckwell, R., and Wolff, E.: Ice drilling on Skytrain Ice Rise and Sherman Island, Antarctica, Ann. Glaciol., 62, 311–323, https://doi.org/10.1017/aog.2021.7, 2021.

NEEM Community Members: Eemian interglacial reconstructed from a Greenland folded ice core, Nature, 493, 489–494, https://doi.org/10.1038/nature11789, 2013.

North Greenland Ice Core Project Members: High-resolution record of Northern Hemisphere climate extending into the last interglacial period, Nature, 431, 147–151, https://doi.org/10.1038/nature02805, 2004.

Nymand, N. F., Radar investigation of the Northeast Greenland Ice Stream: Deriving the crystal orientation fabric, Ph.D. thesis, University of Copenhagen, Denmark, 130 pp., 2024.

Obbard, R. and Baker, I.: The microstructure of meteoric ice from Vostok, Antarctica, J. Glaciol., 53, 41–62, https://doi.org/10.3189/172756507781833901, 2007.

Oswald, G. K. A., Rezvanbehbahani, S., and Stearns, L. A.: Radar evidence of ponded subglacial water in Greenland, J. Glaciol., 64(247), 711-729, https://doi.org/10.1017/jog.2018.60, 2018.

Peters, M. E., Blankenship, D. D., and Morse, D. L.: Analysis techniques for coherent airborne radar sounding: Application to West Antarctic ice streams, J. Geophys. Res., 110, B06303, https://doi.org/10.1029/2004JB003222, 2005.

Petit, J. R., Jouzel, J., Raynaud, D., Barkov, N. I., Delaygue, G., Delmotte, M., Kotlyakov, V. M., Legrand, M., Lipenkov, V. Y., Lorius, C., and Saltzman, E.: Climate and atmospheric history of the past 420,000 years from the Vostok ice core, Antarctica, Nature, 399, 1999.

Porter, C., Morin, P., Howat, I., Noh, M.-J., Bates, B., Peterman, K., Keesey, S., Schlenk, M., Gardiner, J., Tomko, K., Willis, M., Kelleher, C., Cloutier, M., Husby, E., Foga, S., Nakamura, H., Platson, M., Wethington Jr., M., Williamson, C., Bauer, G., Enos, J., Arnold, G., Kramer, W., Becker, P., Doshi, A., D'Souza, C., Cummens, P., Laurier, F., and Bojesen, M.: ArcticDEM, V1 [data set], Harvard Dataverse, https://doi.org/10.7910/DVN/OHHUKH, 2018.

Raynaud, D., Barnola, J.-M., Souchez, R., Lorrain, R., Petit, J.-R., Duval, P., and Lipenkov, V. Y.: The record for marine isotopic stage 11, Nature, 436, 39–40, https://doi.org/10.1038/43639b, 2005.

Rignot, E., Jacobs, S., Mouginot, J., and Scheuchl, B.: Ice-shelf melting around Antarctica, Science, 341(6143), 266-270, https://doi.org/10.1126/science.1235798, 2013.

Ruth, U., Kaufmann, P., Kipfstuhl, S., Lambrecht, A., Morganti, A., Oerter, H., Parrenin, F., Rybak, O., Severi, M., Udisti, R., Wilhelms, F., and Wolff, E.: "EDML1": a chronology for the EPICA deep ice core from Dronning Maud Land, Antarctica, over the last 150 000 years, Clim. Past, 2007.

Saruya, T., Fujita, S., Iizuka, Y., Miyamoto, A., Ohno, H., Hori, A., Shigeyama, W., Hirabayashi, M., and Goto-Azuma, K.: Development of crystal orientation fabric in the Dome Fuji ice core in East Antarctica: implications for the deformation regime in ice sheets, The Cryosphere, 16, 2985–3003, https://doi.org/10.5194/tc-16-2985-2022, 2022.

Saruya, T., Miyamoto, A., Fujita, S., Goto-Azuma, K., Hirabayashi, M., Hori, A., Igarashi, M., Iizuka, Y., Kameda, T., Ohno, H., Shigeyama, W., and Tsutaki, S.: Development of deformational regimes and microstructures in the deep sections and overall layered structures of the Dome Fuji ice core, Antarctica, EGUsphere, 1–48, https://doi.org/10.5194/egusphere-2023-3146, 2024.

Schroeder, D. M., Blankenship, D. D., Raney, R. K., and Grima, C.: Estimating subglacial water geometry using radar bed echo specularity: application to Thwaites Glacier, West Antarctica, IEEE Geosci. Remote Sensing Lett., 12, 443–447, https://doi.org/10.1109/LGRS.2014.2337878, 2015.

Schroeder, D. M., Bingham, R. G., Blankenship, D. D., Christianson, K., Eisen, O., Flowers, G. E., Karlsson, N. B., Koutnik, M. R., Paden, J. D., and Siegert, M. J.: Five decades of radioglaciology, Ann. Glaciol., 61, 1–13, https://doi.org/10.1017/aog.2020.11, 2020.

Souchez, R., Petit, J. R., Jouzel, J., Simões, J., De Angelis, M., Barkov, N., Stievenard, M., Vimeux, F., Sleewaegen, J., and Lorrain, R.: Highly deformed basal ice in the Vostok core, Antarctica, Geophys. Res. Lett., 29, https://doi.org/10.1029/2001GL014192, 2002.

Steig, E. J., Brook, E. J., White, J. W. C., Sucher, C. M., Bender, M. L., Lehman, S. J., Morse, D. L., Waddington, E. D., and Clow, G. D.: Synchronous climate changes in Antarctica and the North Atlantic, Science, 282, 92–95, https://doi.org/10.1126/science.282.5386.92, 1998.

Stillman, D. E., MacGregor, J. a., and Grimm, R. E.: The role of acids in electrical conduction through ice, J. Geophys. Res. Earth Surf., 118, 1–16, https://doi.org/10.1029/2012JF002603, 2013.

Stoll, N., Weikusat, I., Jansen, D., Bons, P., Darányi, K., Westhoff, J., Llorens, M.-G., Wallis, D., Eichler, J., Saruya, T., Homma, T., Drury, M., Wilhelms, F., Kipfstuhl, S., Dahl-Jensen, D., and Kerch, J.: EastGRIP ice core reveals the exceptional evolution of crystallographic preferred orientation throughout the Northeast Greenland Ice Stream, EGUsphere [preprint], https://doi.org/10.5194/egusphere-2024-2653, 2024.

Stoll, N., Westhoff, J., Bohleber, P., Svensson, A., Dahl-Jensen, D., Barbante, C., Weikusat, I.: Chemical and visual characterisation of EGRIP glacial ice and cloudy bands within, The Cryosphere, 17, 2021-2043, https://doi.org/10.5194/tc-17-2021-2023, 2023.

Svensson, A.: Visual stratigraphy of the North Greenland Ice Core Project (NorthGRIP) ice core during the last glacial period, J. Geophys. Res., 110, https://doi.org/10.1029/2004JD005134, 2005.

Takata, M., Iizuka, Y., Hondoh, T., Fujita, S., Fujii, Y., and Shoji, H.: Stratigraphic analysis of Dome Fuji Antarctic ice core using an optical scanner, Ann. Glaciol., 39, 467–472, https://doi.org/10.3189/172756404781813899, 2004.

Thorsteinsson, T., Kipfstuhl, J., and Miller, H.: Textures and fabrics in the GRIP ice core, J. Geophys. Res. Oceans, 102, 26583–26599, https://doi.org/10.1029/97JC00161, 1997.

Tison, J.-L., de Angelis, M., Littot, G., Wolff, E., Fischer, H., Hansson, M., Bigler, M., Udisti, R., Wegner, A., Jouzel, J., Stenni, B., Johnsen, S., Masson-Delmotte, V., Landais, A., Lipenkov, V., Loulergue, L., Barnola, J.-M., Petit, J.-R., Delmonte, B., Dreyfus, G., Dahl-Jensen, D., Durand, G., Bereiter, B., Schilt, A., Spahni, R., Pol, K., Lorrain, R., Souchez, R., and Samyn, D.: Retrieving the paleoclimatic signal from the deeper part of the EPICA Dome C ice core, The Cryosphere, 9, 1633–1648, https://doi.org/10.5194/tc-9-1633-2015, 2015.

Turkeev, A. V., Vasilev, N. I., Lipenkov, V. Y., Bolshunov, A. V., Ekaykin, A. A., Dmitriev, A. N., and Vasilev, D. A.: Drilling the new 5G-5 branch hole at Vostok Station for collecting a replicate core of old meteoric ice, Ann. Glaciol., 62, 305–310, https://doi.org/10.1017/aog.2021.4, 2021.

Verbeke, V., Lorrain, R., Johnsen, S. J., and Tison, J.-L.: A multiple-step deformation history of basal ice from the Dye 3 (Greenland) core: new insights from the CO_2 and CH_4 content, Ann. Glaciol., 35, 231–236, https://doi.org/10.3189/172756402781817248, 2002.

Wang, Y., Thorsteinsson, T., Kipfstuhl, J., Miller, H., Dahl-Jensen, D., and Shoji, H.: A vertical girdle fabric in the NorthGRIP deep ice core, North Greenland, Ann. Glaciol., 35, 515–520, https://doi.org/10.3189/172756402781817301, 2002.

Weikusat, I., Kipfstuhl, S., and Lambrecht, A.: Crystal c-axes (Fabric G20) of Ice Core Samples Collected from the EDML Ice Core with Links to Raw Data Files [data set], https://doi.org/10.1594/PANGAEA.807207, 2013.

868 Weikusat, I., Jansen, D., Binder, T., Eichler, J., Faria, S. H., Wilhelms, F., Kipfstuhl, S., Sheldon, S., Miller, H., Dahl-Jensen,
869 D., and Kleiner, T.: Physical analysis of an Antarctic ice core—towards an integration of micro- and macrodynamics of polar
870 ice, Phil. Trans. R. Soc. Lond. A, 375, 20150347, https://doi.org/10.1098/rsta.2015.0347, 2017.

871 Weikusat, I., Westhoff, J., Kipfstuhl, S., Jansen, D.: Visual stratigraphy of the EastGRIP ice core (14 m - 2021 m depth, drilling
872 period 2017-2019) [data set]. PANGAEA, https://doi.org/10.1594/PANGAEA.925014, 2020.

873 Westhoff, J.: Visual stratigraphy of the EastGRIP ice core: of the lost ice core orientation, deformation structures, extreme
874 warm events, and trapped ancient air, Ph.D. thesis, University of Copenhagen, Denmark, 136 pp., 2021.

875 Wilson, C. J. L., Russell-Head, D. S., and Sim, H. M.: The application of an automated fabric analyzer system to the textural
876 evolution of folded ice layers in shear zones, Ann. Glaciol., 37, 7–17, https://doi.org/10.3189/172756403781815401, 2003.

877 Winter, A., Steinhage, D., Arnold, E. J., Blankenship, D. D., Cavitte, M. G. P., Corr, H. F. J., Paden, J. D., Urbini, S., Young,
878 D. A., and Eisen, O.: Comparison of measurements from different radio-echo sounding systems and synchronization with the
879 ice core at Dome C, Antarctica, The Cryosphere, 11, 653–668, https://doi.org/10.5194/tc-11-653-2017, 2017.

880 Winter, K., Woodward, J., Ross, N., Dunning, S. A., Hein, A. S., Westoby, M. J., Culberg, R., Marrero, S. M., Schroeder, D.
881 M., Sugden, D. E., and Siegert, M. J.: Radar-detected englacial debris in the West Antarctic Ice Sheet, Geophys. Res. Lett.,
882 46, 10454–10462, https://doi.org/10.1029/2019GL084012, 2019.

883 Wolff, E. W.: Electrical stratigraphy of polar ice cores: principles, methods, and findings, in: Physics of Ice Core Records,
884 International Symposium on Physics of Ice Core Records. Shikotsukohan, Hokkaido, Japan, 155–171, 2000.

885 Wolff, E. W., Barbante, C., Becagli, S., Bigler, M., Boutron, C. F., Castellano, E., De Angelis, M., Federer, U., Fischer, H.,
886 Fundel, F., Hansson, M., Hutterli, M., Jonsell, U., Karlin, T., Kaufmann, P., Lambert, F., Littot, G. C., Mulvaney, R.,
887 Röthlisberger, R., Ruth, U., Severi, M., Siggaard-Andersen, M. L., Sime, L. C., Steffensen, J. P., Stocker, T. F., Traversi, R.,
888 Twarloh, B., Udisti, R., Wagenbach, D., and Wegner, A.: Changes in environment over the last 800,000 years from chemical
889 analysis of the EPICA Dome C ice core, Quat. Sci. Rev., 29, 285–295, https://doi.org/10.1016/j.quascirev.2009.06.013, 2010.